Polarization sensitive optical coherence tomography for imaging microvascular information within living tissue without polarization-induced artifacts

PEIJUN TANG AND RUIKANG K. WANG[*] (iD)

Department of Bioengineering, University of Washington, 3720 15th Avenue NE, Seattle, WA 98195, USA
[*]*wangrk@uw.edu*

Abstract: When imaging birefringent samples using optical coherence tomography angiography (OCTA), the phase retardation may appear opposite to the phase change due to the blood flow in the orthogonal signals, for which a cancellation effect can occur when deriving OCTA signals. This effect can diminish the ability of OCTA to detect vascular information, leading to an erroneous interpretation of the final OCTA images. To mitigate this issue, we demonstrate polarization-sensitive optical coherence tomography (PS-OCT) to image microvascular information within a living sample without polarization induced artifacts. The system is furnished with a swept source OCT (SS-OCT) that incorporates two imaging modes: OCTA imaging and polarization-sensitive imaging. PS-OCT is used to provide birefringent contrast where the color-encoded Stokes parameters are used to obtain high contrast polarization-state images. OCTA is used to acquire high-resolution images of functional microvascular networks permeating the scanned tissue volume. Taking the advantages of the dual-channel PS-OCT configuration, the polarization induced artifacts are eliminated from OCTA vascular imaging. The proposed PS-OCTA system is employed to visualize the birefringent components and the vascular networks of the human skin in vivo. It is expected that the proposed system setup would have useful and practical applications in the investigations of the vasculature in the birefringent tissue samples both pre-clinically and clinically.

1. Introduction

A non-invasive tool that integrates complementary imaging contrasts to simultaneously provide the 3D microanatomy and micro-vascular networks within skin tissue is needed for more accurate evaluation of pathological conditions in dermatology, such as skin burn, skin cancer, diabetes and plastic surgery. Optical coherence tomography (OCT) is a non-invasive imaging technique that can generate cross-sectional images of highly scattering sample, enabling the visualization of 3D microstructures with high resolution (1-20 μm) [1]. The functional extensions of OCT: OCT-based vascular imaging (e.g., Doppler OCT [2–4], OCT angiography (OCTA) [5–9]) and polarization sensitive OCT (PS-OCT) [10–14] are the ideal tools, if integrated together, to visualize the depth-resolved vasculature and the birefringent components (tendon, muscle, collagen and nerve fiber bundles) embedded within the skin tissue.

Recently, several dual-modal imaging systems that incorporates Doppler OCT/variance/Correlation-mapping OCTA (cmOCTA) into Jones-matrix PS-OCT have been reported [13,15–19], where both the birefringent and vascular information can be provided simultaneously. However, there are some limitations in these PS-OCT imaging systems. Due to the use of Doppler principle, its sensitivity to blood flow is low that makes it difficult to visualize microcirculations, particularly within the human skin, where the blood flow within the capillary vessels is in an order of 0.1–0.9 mm/s [20]. The cmOCTA can extract the microvascular information but it is sensitive to

the noise in the relatively low backscattering regions [5], which would induce residual background artifacts in the blood flow images.

Optical coherence tomography angiography (OCTA), capable of achieving unprecedented flow sensitivity down to capillary level [5,8], is a promising tool for mapping the high SNR microvasculature within skin. However, there is a potential polarization-induced artifact due to the polarization mismatch between the sample beams and reference beams in the traditional OCTA imaging. Both the system itself and the birefringent sample can generate the polarization artifacts. At the system level, the system-induced polarization artifact, also called the fading effect [21] can be eliminated by carefully aligning the polarization states between the sample and reference beams. However, when imaging the birefringent sample, such pre-alignment treatment is difficult to achieve because the polarization states of the light beams scattered back from the sample are dependent on the un-known birefringent properties of the sample. Both the OCT structural and vascular images can be affected by this problem, but the vascular imaging is affected more seriously. One reason is that the mismatch of the polarization states between the two arms can reduce the signal strength of the coherence signals (i.e. the fading effect) and hence reduce the sensitivity of the OCTA measurement. Another factor that affects the OCTA signal is the phase retardation of the birefringent sample. The birefringent property of the sample may cause two orthogonally polarized rays experiencing different optical path lengths (OPL) or phase retardation. In the traditional OCT, only the projections of the two orthogonally polarized rays onto the polarized direction of the reference light are detected. Due to the phase retardation between the two rays, the phase shift due to the blood flow can appear as an opposite change in the orthogonal signals, for which a cancellation effect can occur when deriving OCTA signals. This effect can diminish the ability of OCTA to detect vascular information, leading to erroneous interpretation of the final OCTA images. Note that, other imaging modalities such as speckle-variance and correlation-mapping OCTA that only utilize intensity to extract the vascular signals could be affected less by the polarization-induced cancellation effect. To mitigate this issue, the two orthogonal states of light emerging from the birefringent sample must be detected separately. For doing so, PS-OCT imaging configuration would be ideal.

In this study, we propose a dual-functional imaging system that integrates PS-OCT with the OCTA setup to provide polarization-artifact (PA) free microvascular images as well as high contrast birefringent images of the skin. OCTA images are acquired from two channels in the PS-OCT configuration, respectively, which are then combined to generate the final PA-free OCTA image. For polarization sensitive imaging, the algorithm of color-encoded approach [14] is used to obtain high contrast polarization-state images, in which three primary colors of red, green, and blue are used to code Stokes parameters of Q, U, and V, respectively. With this method, the comprehensive birefringent information (i.e. the phase retardation and three-dimensional axis orientation) can be presented simultaneously in one color image with high contrast. Unlike the previous studies [22] that deduce stoke vectors which are difficult to provide one-to-one correspondence between the polarization state and the measured value, the color-encoded parameter can present a unique polarization state with a unique color in the image. The proposed dual-functional PS-OCTA imaging system is demonstrated by in vivo imaging of human tissue to visualize its birefringent information and microvascular networks.

2. Materials and methods

2.1. Dual-functional optical coherence tomography imaging system

Schematic setups for the dual-functional PS-OCTA and a traditional OCT are shown in Fig. 1, where a swept source configuration is implemented. Both systems used a 100-kHz MEMS-VCSEL swept laser source (SL1310V1-20048, Thorlabs), providing an output power of 25 mW with a central wavelength of 1310 nm and a spectral tuning range of 100 nm. For PS-OCTA imaging (Fig. 1(a)), the output of the light source was sent to a polarization controller and became linearly

polarized through a polarization beam splitter (PBS 1) (PFC1310A, Thorlabs), and then split into the reference and the sample arms through a PM coupler (PN1310R5A2, Thorlabs) at a split-ratio of 50:50. The reference arm was installed with a quarter-wave plate (QWP) with its axis aligned at 22.5° with reference to the input polarization state, ensuring that the reflected light was coupled equally into the vertical and horizontal channels. The sample arm was equipped with a QWP aligned at 45° with respect to the input polarization state, which makes the linearly polarized light to become a circularly polarized light before illuminating the sample. The lights coming back from both the reference and sample arms were recombined and sent to the PBS1 and PBS2, respectively, where the interference light was split into horizontal (Channel 1) and vertical (Channel 2) components. Balanced detection was used for both vertical and horizontal channels to collect the interference signals, upon which to reconstruct the OCTA and PS-OCT images simultaneously.
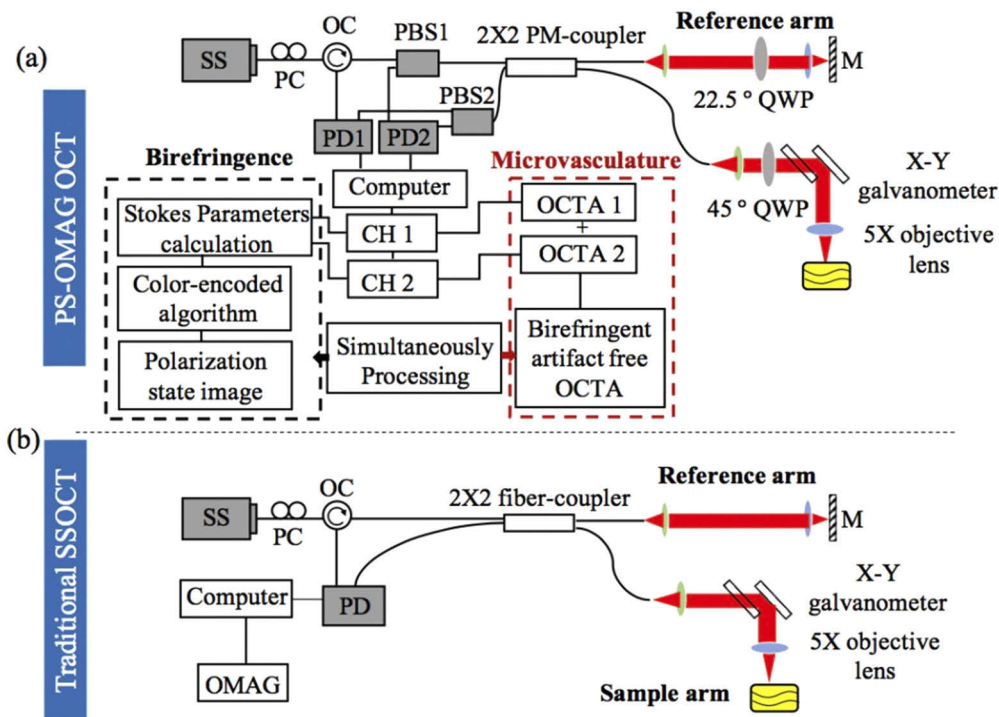
Fig. 1. Schematic of (a) dual modality PS-OCTA system and (b) the traditional SS-OCT system. SS: swept source; PC: polarization controller; OC: optical circulator; PBS: polarization beam splitter; PM-coupler: polarization maintaining coupler; QWP: quarter wave plate; PD: photo detector; CH: channel. OCTA: optical coherence tomography angiography via OMAG algorithm. Data processing flow chart of the dual modality imaging system is also shown in (a).

In order to show the advantages of the PS-OCTA, we also established a traditional OCT system (Fig. 1(b)) for the purpose of comparison of imaging performances. In this system, the output of the light source was sent to a polarization controller, and then split into the reference and the sample arms through a normal fiber coupler at a split-ratio of 50:50. The lights coming back from both reference and sample arms were recombined and sent to the photodetector, where balanced detection was employed to collect the interference signals that were used to reconstruct the traditional OCTA images.

2.2. Imaging protocol

We used a same imaging protocol for both the systems. Briefly, to image the capillary level microvasculature, ultrahigh sensitive OMAG scanning protocol was adopted [8]. Each B-scan contained 400 A-lines with 180 Hz framerate. 400 B-scan locations with 7 repeated B scans at each location were acquired to form the 3D imaging data. Thus, each data set contained 1,120,000 A-lines, taking 15.4 s to acquire.

For PS-OCTA imaging, complex OCT image $C_{H,V}(x, y, z) = A_{H,V}(x, y, z)e^{\varphi_{H,V}(x,y,z)}$ was first reconstructed following traditional OCT processing, where $A_{H,V}(x, y, z)$ is the magnitude used to produce the conventional structural images, $\varphi_{H,V}(x, y, z)$ is the phase signal caused by the microstructures located at the depth z. The subscripts H and V denote the horizontal and vertical channels, respectively. Then the PA-free OCTA image and the PS-OCT image are both obtained in parallel from this complex image.

To realize OCTA, the OMAG algorithm was applied to each channel to extract the blood flow information within the scanned tissue. The intensity of the blood flow image was calculated by the following equation:

$$I_{H,V}^{OMAG}(x, y, z) = [1 - Norm(\overline{I_{H,V}(x, y, z)})]\frac{1}{N-1}\sum_{i=1}^{N-1}|C_{H,V}^{i+1}(x, y, z) - C_{H,V}^i(x, y, z)|, \quad (1)$$

where $I_{H,V}(x, y, z)$ is the OCT structural signal; $C_{H,V}^i(x, y, z)$ is the complex OCT signal containing both amplitude and phase information in the i' th repeated B-scan, N is the number of B-scan repetitions, $Norm(\overline{I(x, y, z)})$ is the normalized structural signals which brings the values in the image to a range between 0 and 1, which helps remove the hyper-reflection artifacts. The PA-free OCTA image $I_{OMAG}(x, y, z)$ was obtained by:

$$I_{OMAG}(x, y, z) = \sqrt{I_H^{OMAG}(x, y, z)^2 + I_V^{OMAG}(x, y, z)^2}. \quad (2)$$

To obtain PS-OCT images, Stokes parameters (I, Q, U and V) were calculated by:

$$
\begin{aligned}
I &= A_H(x, y, z)^2 + A_V(x, y, z)^2 \\
Q &= A_H(x, y, z)^2 - A_V(x, y, z)^2 \\
U &= 2(A_H(x, y, z)A_V(x, y, z)\cos(\varphi_V(x, y, z) - \varphi_H(x, y, z)) \\
V &= 2(A_H(x, y, z)A_V(x, y, z)\sin(\varphi_V(x, y, z) - \varphi_H(x, y, z)).
\end{aligned}
\quad (3)
$$

The primary colors of red, green and blue were used to code each Stokes parameter of Q, U and V, respectively, to result in one final image for the visualization of the polarization state, representing the birefringent property of the probed sample. A Poincaré sphere whose surface represents all the polarization states is color-encoded by this method [14], where the phase retardation $\delta(x, y, z) = tan^{-1}\left[\frac{A_H(x,y,z)}{A_V(x,y,z)}\right]$ and the relative orientation of the optic axis $\theta(x, y, z) = \frac{\varphi_V(x,y,z) - \varphi_H(x,y,z)}{2}$ [23].

2.3. Cause and removal of the polarization-induced artifacts in OCTA

The generation and removal of the polarization-induced artifacts in the microvascular imaging are discussed below. To consider the polarization property of the probing light in the OCT imaging, we consider the two orthogonal rays whose difference is the phase retardation. Note that in the absolute coordinate system, the direction of these two orthogonal polarized rays is determined by the orientation of the birefringent sample. Since the polarization state of the reference beam is constant, the projection values of the reference beams onto these two rays are dependent on the orientation of optic axis of the sample, which is un-known and varies from region to region. This is why the sample-induced polarization artifact is inevitable in the traditional OCT system. When

the polarization direction of the reference beam is parallel to the horizontal ray, the coherent interference in the vertical direction would be totally lost, and vice versa. As a result, the signal strength and the sensitivity of the blood flow will be reduced. In this case, the PA is introduced by the orientation of the sample rather than the phase retardation of the sample. This is the first type of the sample-induce PA.

The phase retardation can also induce another type of PA. In this case, the reference beam is not parallel to each of the rays. As orthogonal polarizations are independent, the coherence signal in each polarized ray can be evaluated independently. In the traditional OCT, the detected interference signal $I(\omega, \Delta z)$ is the superposition of the coherence signals at each polarized ray, i.e., $I(\omega, \Delta z) = 2E_{rH}E_{sH}\cos(2kn_Hz) + 2E_{rV}E_{sV}\cos(2kn_Vz)$, where $E_{H,V}$ is the backscattering from the reference and sample, $k = 2\pi/\lambda$ the wavenumber, $n_{H,V}$ the refractive index of the birefringent sample corresponding to each polarized direction. Complex depth-resolved signal $C(z)$ can be reconstructed by performing the Fourier transformation on $I(\omega, \Delta z)$: $C(z) = A_H(z)e^{i\varphi_H(z)} + A_V(z)e^{i\varphi_V(z)}$, where $A_{H,V}(z)$ is the magnitude used to produce the conventional OCT structural images, $\varphi_{H,V}(z)$ is the phase signal at the depth z. When there is blood flow within birefringent tissue, both the motion of the red blood cells (RBCs) and the birefringence of the tissue can induce phase shifts. The phase shift due to the blood flow $\varphi_b(z, t)$ is equal in both the polarized planes assuming the RBCs are non-birefringent. However, the phase shift due to the tissue birefringence generates a phase retardation $\varphi_t(z)$ between the orthogonal polarized planes. $\varphi_b(z, t)$ is time-dependent, whereas $\varphi_t(z)$ is constant. Hence, the corresponding complex depth-resolved signal $C(z, t)$ can be expressed as

$$C(z, t) = A_H(z)e^{i[\varphi_H(z)+\varphi_b(z,t)]} + A_V(z)e^{i[\varphi_H(z)+\varphi_t(z)+\varphi_b(z,t)]}. \tag{4}$$

The OCTA signal can be expressed as:

$$I_{OMAG}(z) = [1 - Norm(\overline{I(z)})]\frac{1}{N-1}\sum_{i=1}^{N-1}|\Delta C_H(z) + \Delta C_V(z)|, \tag{5}$$

where $\Delta C_{H,V}(z)$ represents the difference of the complex signals $C_{H,V}(z)$ between two successive B-scans. When $\varphi_t(z)$ is near the integral multiple of π, two effects can be expected. First, the complex signal $C(z, t)$ is diminished because the signals from the two orthogonal planes could cancel each other, which is the fading effect as discussed in the previous study [21]. Second, the OCTA signal determined by the difference between adjacent complex signals can also be obscured because the phase shift due to the blood flow may appear as an opposite change in the orthogonal signals (i.e. $\Delta C_H(z)*\Delta C_V(z)<0$), for which a cancellation effect can occur when calculating OCTA signals. In practice, $\varphi_t(z)$ can be any value. Compared to the extreme cases above, the cancellation effect decreases in various degrees but still exists and affects the OCTA signals. For these reasons, the microvascular information can be obscured in the OCTA images of the birefringent tissue. By using the PS-OCT detection configuration, the orthogonal polarized light beams are detected separately. The OCTA signals could be calculated in each channel (Eq. (1)), which are then combined as shown in Eq. (2). In this way, the cancellation effect can be avoided, resulting in PA-free OCTA images.

3. Results and discussion

To demonstrate that the dual-functional PS-OCTA imaging system can provide the PA-free microvascular images, we conducted the in vivo OCTA imaging of human skin tissue. For comparison, we also performed traditional OCTA imaging. Here the highly birefringent palm skin of a healthy volunteer's right hand was selected for demonstration. To enhance the imaging depth, a drop of the glycerol solution covered with a thin glass slide was applied on the skin surface for refractive index matching [24]. We employed an objective lens with 36 mm focal

length, which provided ~20 μm lateral resolution. The sampling spacing in the scanning was 10 μm in X and Y directions for a fine visualization of both the structure and vasculature of human skin. Field of view of the images was 8×8 mm^2. To ensure the area imaged by both systems (Fig. 1) was the same, we marked the target skin area with a very small piece of tape that was used the guide to align the system scanning during imaging.

Figure 2 shows the OCTA and the structural OCT images captured by both the systems. In the structural OCT image (Figs. 2(e)–2(g), shown in cross-sectional structural images), the stratum corneum is well delineated. The thickness of the stratum corneum was measured to be ~200 μm, within which the blood vessels are devoid as evidenced by the cross-sectional OCTA images in Figs. 2(a)–2(d). Right beneath the stratum corneum, the blood vessel networks appear. Note that the triangular shape appearing at the lower right corner is the imaging guidance marker that was used to guide the imaging of the two systems to target the same area. Figure 2(a) is the traditional en face maximum intensity projection (MIP) microvascular image with depth-color encoding to appreciate the depth location of the blood vessels, where microvasculature can be visualized as expected. The shown depth was ~2 mm. The red color codes the deeper vessels while the green color denotes the shallow vessels. However, there appears some dark bands where the OCTA signal strengths are relatively weak (e.g. in the bottom region). It can be seen that the orientation of the dark bands is approximately perpendicular to the orientation of the fingerprint. We selected the B-scan frame across the dark band and show this B-scan cross-sectional OCTA image in Fig. 2(a), where the microvascular signals appear less abundant in this region. Vessel density (VD) within selected areas (2×2 mm^2) in the en face image as indicated by the yellow and red boxes in Fig. 2(a) was calculated [25], which would expect to deliver a similar value due to relatively uniform distribution of vascularity in this healthy palm skin. However, the VD values in the upper and bottom box-region are 43% and 37% respectively, showing that part of the vascular signals in the bottom region are obscured by the PA due to the birefringence of the tissue. These results show possible erroneous interpretation of conventional OCTA images.

Figures 2(b) and 2(c) show the en face MIP microvascular image with depth-color encoding acquired from the two orthogonal polarized channels (Channel 1 and Channel 2) in the PS-OCTA system respectively. It appears that the two orthogonal polarization states provide anatomically distinct blood vessel networks which are located at different physical depths within the birefringent skin. Together with polarization sensitive images (Fig. 3, see below), blood vessels along with the ridges of the fingerprint can be easily visualized in Channel 1 whereas it is hard to appreciate in the Channel 2. Channel 2 shows strong blood vessels signals that appear relatively weak in the Channel 1. The opposite trend in the OCTA signals in horizontal and vertical channels agree well with the polarization theoretical framework, demonstrating that the mismatch of the polarization states of the reference beam and the sample beam can obscure blood flow signals. However, the two orthogonal polarized channels can provide complementary OCTA signals. The OCTA signals diminished by the PA in one channel can be captured by the other channel. Hence, combining the OCTA images in the two channels can help to remove the polarization induced artifacts.

Figure 2(d) shows the PA-free OCTA images and the corresponding cross-sectional image, respectively, where the abundant blood vessel information is provided without the dark band generated due to the PA as shown in Fig. 2(a). The missing (or attenuated) vascular information in either Figs. 2(b) or 2(c) are now recovered in Fig. 2(d) because the complementary information was combined. The cross-sectional image in Fig. 2(d) provide the abundant vessels information in the region where the OCTA signals are diminishing due to the PA in the Fig. 2(a). The average VD values in the upper and bottom regions indicated by the red and yellow boxes are 45% and 46%, respectively, which is expected from the uniform distribution of vascularity in this healthy palm skin. These results demonstrate that polarization induced artifacts can be avoided
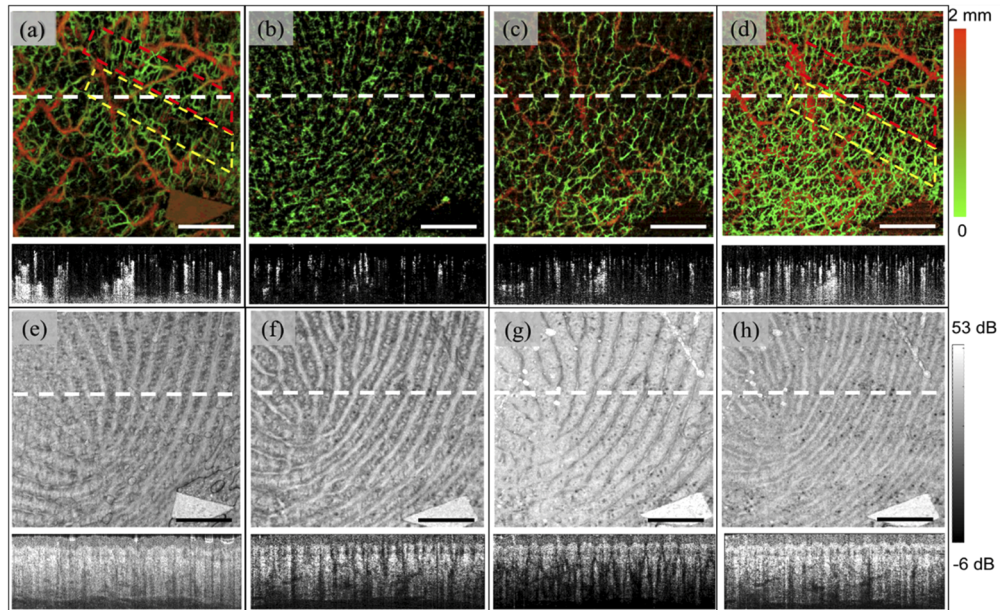
Fig. 2. The OCTA and OCT structure results obtained from a birefringent skin tissue (palm). The microvascular OCTA en face image and the cross-sectional image corresponding to the position indicated by the white dash line resulted from (a) the traditional SS-OCT; (b) and (c) the horizontal (CH 1) and vertical channels (CH 2) of the PS-OCTA imaging system. (d) The PA-free microvascular OCTA en face image and the corresponding cross-sectional image. The structural OCT en face image and the cross-sectional image corresponding to the position indicated by the white dash line resulted from (e) the traditional SS-OCT; (f) and (g) the horizontal (CH 1) and vertical channels (CH 2) of the PS-OCT imaging system. (h) The combination structural en face image and the corresponding cross-sectional image. The scale bar is 2 mm.
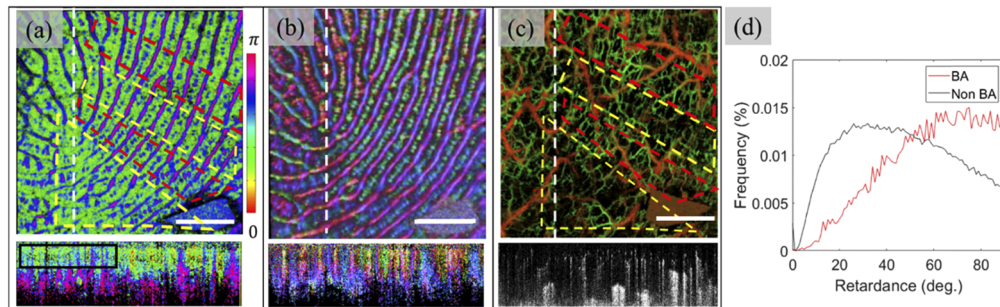
Fig. 3. Volumetric polarization state images of healthy palm skin in vivo. a) Images resulted from using phase retardation as the imaging parameter; b) Results using the polarization sate as the imaging parameter; c) Traditional OCTA en face image. d) The histogram distributions of retardation values obtained from the ROI indicated by the yellow (PA region) and red box (non-PA region) in (a) and (c), respectively. The scale bar = 2 mm.

by combining the OCTA images captured by the orthogonal polarized channels in PS-OCTA system.

The advantage of PS-OCTA is that the polarization sensitive images of the scanned tissue volume can also be obtained in parallel in addition to the PA-free OCTA images. We used the same dataset in Fig. 2 to obtain the 3D images and corresponding cross-sectional images of the phase retardation (Fig. 3(a)) and polarization state images (Fig. 3(b)). The PS-OCT images in Figs. 3(a) and 3(b) are the 3D volume images created by the software ImagJ. In doing so, we first flattened the volume with reference to the surface of the tissue, and then removed the superficial stratum corneum layer (∼100 μm) with low birefringence. The birefringent material that gives rise to the measured retardance could be due to the fibrillar dermal collagen. The estimated birefringence of the dermal collagen is around ∼0.3° μm⁻¹ [26] and hence the physical distance required to accumulate the pi phase difference between orthogonal states should be around 300 μm. To demonstrate that the phase retardation of the sample can induce the PA, the distributions of the phase retardation values obtained from the PA regions (indicated by the yellow boxes in Figs. 3(a) and 3(c)) and the non-PA regions (indicated by the red boxes in Figs. 3(a) and 3(c)) are shown in the histogram in Fig. 3(d).

For comparison, the traditional OCTA results (Fig. 3(c)) is also presented to show how the birefringent property would affect the OCTA signals. In the traditional OCTA 3D image (Fig. 3(c)), the regions where the vascular signals are relatively weak are indicated by the dashed yellow outlines. In these regions, the dominate color in the phase retardation image (Fig. 3(a)) is green (∼75°-90°) as shown in the histograms in Fig. 3(d) while other regions have lower phase retardation values (∼20°-60°). Due to round-trip measurement, the phase delay between the two orthogonal rays scattered back from this region is close to pi, which can diminish the OCTA signals and generate the PA. The cross-sectional images were selected at the region indicated by the white dash lines in Figs. 3(a)–3(c). In the cross-sectional image in Fig. 3(a), the average phase retardation value of the region indicated by the black box is around 86.7°, which is responsible for causing the PA. In this region, the blood vessels signals, especially the microvascular signals are relatively weak as shown in the cross-sectional images in Fig. 3(c), demonstrating that vascular signals are diminishing by the phase retardation induced PA.

The polarization sensitive results (Figs. 3(a) and 3(b)) show the architecture that resembles the fingerprint features of the human palm skin. In the phase retardation image (Fig. 3(a)), the ridges and papillae can be approximately appreciated. The phase retardation values of the ridges and papillae are close (with average values of 2.88 (rad.) and 2.76 (rad.), respectively). Figure 3(b) shows that polarization state image of the sample provides a comprehensive and un-ambiguous image in visualizing the architecture of the human palm skin. In the polarization state image, the amorphous components within the tissue can be removed easily [14], and therefore the texture of the strong birefringent component: the papillae and the ridges can be extracted and differentiated. The texture structure shows the collagen organizations between the papillae and ridges are cross-type.

While we have demonstrated the usefulness of the proposed PS-OCTA imaging system, further improvement is required to include treatments that reduce the artifacts induced by the cross-coupling between orthogonal polarization modes within the PM fibers. This cross-coupling effect in the PM fibers could make vertical offset copies of the OCT image appearing above and below the real sample, potentially degrading the image quality and affecting quantitative measurements of the tissue birefringence and blood flow. There are two potential solutions to mitigate this issue: 1) using a long PM fiber segment to displace the artifacts out of the OCT ranging distance [27]; and 2) using the wavelet-FFT filtering post-processing algorithm to remove the artifacts [28]. In doing so, more accurate quantitative measurements of the polarization parameters and blood flow information can be obtained in parallel, useful for assessing pathological states of the sample, for example in the assessment of the burn pathological models in the course of disease development.

4. Conclusion

In conclusion, we have demonstrated a dual functional PS-OCTA imaging system that can provide 3D polarization-artifact free microvascular images and high contrast polarization sensitive images simultaneously with one measurement. We have experimentally shown that by utilizing the detections in the orthogonal channels of the PS-OCT configuration, the polarization-induced artifacts in the OCTA images can be avoided. It is hoped that the proposed PS-OCTA imaging would be useful in the practical investigations of microvascular and birefringent tissue involvements in the disease development both pre-clinically and clinically.

Funding

Disclosures

The authors declare no conflicts of interest.

References

1. P. H. Tomlins and R. K. Wang, "Theory, developments and applications of optical coherence tomography," J. Phys. D: Appl. Phys. **38**(15), 2519–2535 (2005).
2. J. A. Izatt, M. D. Kulkarni, S. Yazdanfar, J. K. Barton, and A. J. Welch, "In vivo bidirectional color Doppler flow imaging of picoliter blood volumes using optical coherence tomography," Opt. Lett. **22**(18), 1439–1441 (1997).
3. Z. Chen, T. E. Milner, D. Dave, and J. S. Nelson, "Optical Doppler tomographic imaging of fluid flow velocity in highly scattering media," Opt. Lett. **22**(1), 64–66 (1997).
4. J. You, A. Li, C. Du, and Y. Pan, "Volumetric Doppler angle correction for ultrahigh-resolution optical coherence Doppler tomography," Appl. Phys. Lett. **110**(1), 011102 (2017).
5. C.-L. Chen and R. K. Wang, "Optical coherence tomography based angiography [Invited]," Biomed. Opt. Express **8**(2), 1056–1082 (2017).
6. R. K. Wang, S. L. Jacques, Z. Ma, S. Hurst, S. R. Hanson, and A. Gruber, "Three dimensional optical angiography," Opt. Express **15**(7), 4083–4097 (2007).
7. J. Fingler, R. J. Zawadzki, J. S. Werner, D. Schwartz, and S. E. Fraser, "Volumetric microvascular imaging of human retina using optical coherence tomography with a novel motion contrast technique," Opt. Express **17**(24), 22190–22200 (2009).
8. L. An, J. Qin, and R. K. Wang, "Ultrahigh sensitive optical microangiography for in vivo imaging of microcirculations within human skin tissue beds," Opt. Express **18**(8), 8220–8228 (2010).
9. R. K. Wang, L. An, P. Francis, and D. J. Wilson, "Depth-resolved imaging of capillary networks in retina and choroid using ultrahigh sensitive optical microangiography," Opt. Lett. **35**(9), 1467–1469 (2010).
10. J. F. de Boer, T. E. Milner, M. J. C. van Gemert, and J. S. Nelson, "Two-dimensional birefringence imaging in biological tissue by polarization-sensitive optical coherence tomography," Opt. Lett. **22**(12), 934–936 (1997).
11. C. Fan, Y. Wang, and R. K. Wang, "Spectral domain polarization sensitive optical coherence tomography achieved by single camera detection," Opt. Express **15**(13), 7950–7961 (2007).
12. H. Wang, T. Akkin, C. Magnain, R. Wang, J. Dubb, W. J. Kostis, M. A. Yaseen, A. Cramer, S. Sakadžić, and D. Boas, "Polarization sensitive optical coherence microscopy for brain imaging," Opt. Lett. **41**(10), 2213–2216 (2016).
13. Y. Lim, Y.-J. Hong, L. Duan, M. Yamanari, and Y. Yasuno, "Passive component based multifunctional Jones matrix swept source optical coherence tomography for Doppler and polarization imaging," Opt. Lett. **37**(11), 1958–1960 (2012).
14. P. Tang, J. Xu, and R. K. Wang, "Imaging and visualization of the polarization state of the probing beam in polarization-sensitive optical coherence tomography," Appl. Phys. Lett. **113**(23), 231101 (2018).
15. E. Li, S. Makita, Y.-J. Hong, D. Kasaragod, and Y. Yasuno, "Three-dimensional multi-contrast imaging of in vivo human skin by Jones matrix optical coherence tomography," Biomed. Opt. Express **8**(3), 1290–1305 (2017).
16. K. S. Park, W. J. Choi, S. Song, J. Xu, and R. K. Wang, "Multifunctional in vivo imaging for monitoring wound healing using swept-source polarization-sensitive optical coherence tomography," Lasers Surg Med **50**(3), 213–221 (2018).
17. B. Braaf, S. Donner, A. S. Nam, B. E. Bouma, and B. J. Vakoc, "Complex differential variance angiography with noise-bias correction for optical coherence tomography of the retina," Biomed. Opt. Express **9**(2), 486–506 (2018).
18. P. Gong, Q. Li, Q. Wang, K. Karnowski, and D. D. Sampson, "Jones matrix-based speckle-decorrelation angiography using polarization-sensitive optical coherence tomography," J. Biophotonics **13**(9), e202000007 (2020).
19. P. Gong, L. Chin, S. Es'haghian, Y. M. Liew, F. Wood, D. Sampson, and R. McLaughlin, "Imaging of skin birefringence for human scar assessment using polarization-sensitive optical coherence tomography aided by vascular masking," J. Biomed. Opt. **19**(12), 126014 (2014).

20. M. Stücker, V. Baier, T. Reuther, K. Hoffmann, K. Kellam, and P. Altmeyer, "Capillary blood cell velocity in human skin capillaries located perpendicularly to the skin surface: measured by a new laser doppler anemometer," Microvasc. Res. **52**(2), 188–192 (1996).

21. N. Wang, X. Liu, Q. Xiong, J. Xie, S. Chen, and L. Liu, "Polarization management to mitigate misalignment-induced fringe fading in fiber-based optical coherence tomography," Opt. Lett. **42**(15), 2996–2999 (2017).

22. G. Peijun, C. Lixin, E. H. Shaghayegh, L. Yih Miin, M. W. M. D. Fiona, D. S. David, and A. M. Robert, "Imaging of skin birefringence for human scar assessment using polarization-sensitive optical coherence tomography aided by vascular masking," J. Biomed. Opt. **19**(12), 126014 (2014).

23. C. K. Hitzenberger, E. Götzinger, M. Sticker, M. Pircher, and A. F. Fercher, "Measurement and imaging of birefringence and optic axis orientation by phase resolved polarization sensitive optical coherence tomography," Opt. Express **9**(13), 780–790 (2001).

24. R. K. Wang, X. Xu, V. V. Tuchin, and J. B. Elder, "Concurrent enhancement of imaging depth and contrast for optical coherence tomography by hyperosmotic agents," J. Opt. Soc. Am. B **18**(7), 948–953 (2001).

25. S. J. Men, C.-L. Chen, W. Wei, T.-Y. Lai, S. Z. Song, and R. K. Wang, "Repeatability of vessel density measurement in human skin by OCT-based microangiography," Skin. Res. Technol. **23**, 607–612 (2017).

26. S. Sakai, M. Yamanari, A. Miyazawa, M. Matsumoto, N. Nakagawa, T. Sugawara, K. Kawabata, T. Yatagai, and Y. Yasuno, "In vivo three-dimensional birefringence analysis shows collagen differences between young and old photo-aged human skin," J. Invest. Dermatol. **128**(7), 1641–1647 (2008).

27. M. K. Al-Qaisi and T. Akkin, "Polarization-sensitive optical coherence tomography based on polarization-maintaining fibers and frequency multiplexing," Opt. Express **16**(17), 13032–13041 (2008).

28. R. Byers and S. Matcher, "Attenuation of stripe artifacts in optical coherence tomography images through wavelet-FFT filtering," Biomed. Opt. Express **10**(8), 4179–4189 (2019).